Currents, drag, and sediment transport induced by a tsunami

Jessica R. Lacy,[1] David M. Rubin,[1] and Daniel Buscombe[2]

Received 2 February 2012; revised 22 June 2012; accepted 9 August 2012; published 22 September 2012.

[1] We report observations of water surface elevation, currents, and suspended sediment concentration (SSC) from a 10-m deep site on the inner shelf in northern Monterey Bay during the arrival of the 2010 Chile tsunami. Velocity profiles were measured from 3.5 m above the bed (mab) to the surface at 2 min intervals, and from 0.1 to 0.7 mab at 1 Hz. SSC was determined from the acoustic backscatter of the near-bed profiler. The initial tsunami waves were directed cross shore and had a period of approximately 16 min. Maximum wave height was 1.1 m, and maximum current speed was 0.36 m/s. During the strongest onrush, near-bed velocities were clearly influenced by friction and a logarithmic boundary layer developed, extending more than 0.3 mab. We estimated friction velocity and bed shear stress from the logarithmic profiles. The logarithmic structure indicates that the flow can be characterized as quasi-steady at these times. At other phases of the tsunami waves, the magnitude of the acceleration term was significant in the near-bed momentum equation, indicating unsteady flow. The maximum tsunami-induced bed shear stress (0.4 N/m^2) exceeded the critical shear stress for the medium-grained sand on the seafloor. Cross-shore sediment flux was enhanced by the tsunami. Oscillations of water surface elevation and currents continued for several days. The oscillations were dominated by resonant frequencies, the most energetic of which was the fundamental longitudinal frequency of Monterey Bay. The maximum current speed (hourly-timescale) in 18 months of observations occurred four hours after the tsunami arrived.

Citation: Lacy, J. R., D. M. Rubin, and D. Buscombe (2012), Currents, drag, and sediment transport induced by a tsunami, *J. Geophys. Res.*, *117*, C09028, doi:10.1029/2012JC007954.

1. Introduction

[2] Over the past decade measurements of tsunamis have proliferated, documenting both their propagation across the ocean and conditions at landfall. However, these data are almost exclusively records of water surface elevation, with very few measurements of current speed. Tsunamis traveling across the deep ocean have small amplitudes and negligible currents, but as they move into shallow coastal waters, wave height and current speed increase. While inundation is the most obvious hazard associated with tsunamis, the drag force, which is proportional to velocity squared, carries much greater potential for destruction [*Yeh*, 2006]. Thus, measurement and accurate prediction of the currents generated by tsunamis is an important component of hazard assessment. Previously, *Bricker et al.* [2007] published tsunami current data measured under relatively small oscillations in water surface elevation (<0.17 m), and *Lynett et al.* [2012] reported currents generated by the 2011 Tohoku tsunami at two remote locations. In addition, overland current speeds have been estimated from survivor videos taken during the Tohoku and Samoa tsunamis [*Fritz et al.*, 2006, 2012].

[3] Modeling of tsunami propagation across the ocean neglects friction, which is reasonable in deep water, where the bottom boundary layer is a very small fraction of the depth. As the tsunami approaches shore this fraction increases, both because the ambient depth decreases and because current speed and thus bed friction increase. The potential for bed drag to influence tsunami-generated currents is much greater than for wind waves, because tsunami periods are an order of magnitude longer. Measurements of currents in the bottom boundary layer under tsunamis are critical for evaluating the treatment of bed friction in models of tsunamis as they approach shore. They are also needed to determine bed shear stress and estimate sediment mobilization by tsunamis, and can contribute to accurate hindcasting of tsunami currents from characteristics of sedimentary deposits, an important goal of paleo-tsunami research [*Huntington et al.*, 2007].

[4] Tsunamis can cause damage far from their source, and much of the damage is due to currents [*Lynett et al.*, 2012]. The potential for tsunamis to initiate seiching (free-surface oscillations in enclosed basins) in harbors and bays has long been known [*Miles*, 1974; *Murty*, 1977]. Coupling between the initial tsunami forcing and local resonance produces variation in tsunami signals along a coast, and can lead to

[1]U.S. Geological Survey, Santa Cruz, California, USA.
[2]School of Marine Science and Engineering, University of Plymouth, Plymouth, UK.

Corresponding author: J. R. Lacy, U.S. Geological Survey, Pacific Coastal and Marine Science Center, 400 Natural Bridges Drive, Santa Cruz, CA 95060, USA. (jlacy@usgs.gov)

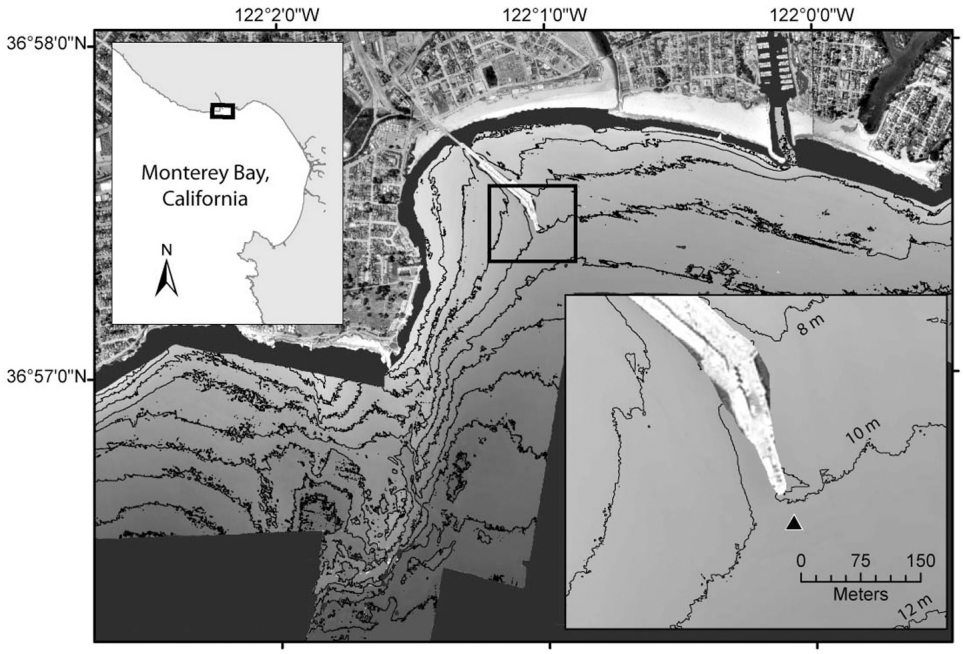

Figure 1. Study site in northern Monterey Bay, CA, with bathymetric contours at 2-m intervals. Triangle in inset indicates tripod location, south of the end of the Santa Cruz wharf.

local enhancement of tsunamis [*Tang et al.*, 2008; *Munger and Cheung*, 2008; *Dengler et al.*, 2009]. Narrow harbors are particularly susceptible to damaging current surges produced by remote tsunamis. The 2011 Tohoku tsunami caused significant damage in the harbors of Crescent City and Santa Cruz, California, as well as Brookings, Oregon [*Allan et al.*, 2012]; and Crescent City has repeatedly been impacted by tsunamis [*Dengler et al.*, 2009]. Accurate prediction of harbor and bay responses to tsunamis requires understanding the transformation of currents generated by tsunamis as they traverse the inner shelf.

[5] Although the amplitudes of far-field tsunamis are commonly no greater than the local tidal range or maximum wave heights, the periods of tsunami are quite different from these other types of oscillations. As a result, at coastal sites with relatively weak tidal currents, far-field tsunamis have the potential to create unusually strong pulses of mixing, transport, and bed mobilization that may affect both benthic and pelagic ecosystems.

[6] In this paper we describe the currents and suspended sediment transport associated with the arrival in Monterey Bay, California, of the 2010 tsunami originating in Chile, as well as the subsequent seiching. The tsunami was caused by a magnitude 8.8 earthquake with epicenter offshore of Maule, Chile, occurring at 06:34 on 27 February 2010 UT (www.quake.usgs.gov;nctr.pmel.noaa.gov/chile20100227). It arrived in Monterey Bay approximately 14 hours later. Water surface elevation, currents, and suspended sediment concentrations (SSC) were measured on the inner shelf in northern Monterey Bay. The data set includes profiles of velocity and SSC in the meter above the seafloor. We evaluate terms in the momentum equation during the initial tsunami oscillations, and show that the flow alternated between unsteady and quasi-steady. We estimate tsunami-generated bed shear stress for periods of quasi-steady flow during the largest tsunami wave, and find that it exceeded the critical shear stress. The influence of the tsunami on SSC could not be distinguished, because the bed shear stress due to surface waves was much greater than that of the tsunami, but the tsunami clearly enhanced cross-shore sediment flux. Sediment flux in the along-shore direction continued to be elevated during the seiche that persisted for several days after the tsunami arrived. We identify frequencies of oscillation in both water surface elevation and currents during this period using singular spectrum analysis, to determine the influence of seiching on currents.

2. Methods

2.1. Study Site

[7] The study site was located on the inner shelf of northern Monterey Bay (36.95690°N 122.01700°E), 40 m south of the end of the Santa Cruz wharf at a depth of 10 m relative to mean-lower-low water (MLLW) (Figure 1). Tidal range is 1.63 m during spring tides, and tidal currents are typically very weak, with magnitudes less than 0.05 m/s. Bed sediments are medium-grained sand. In late February 2010, grain size was 315 $\pm$ 120 μm (mean $\pm$ s.d.), based on hourly measurements using digital images (D. Buscombe at al., manuscript in preparation, 2012).

2.2. Data Collection and Processing

[8] The data reported here were collected as part of a long-term deployment designed to investigate wave-driven sediment dynamics. Instruments mounted on a tripod on the seafloor were connected by ethernet cable to a PC on the Santa Cruz wharf, allowing control of the instruments and transmission of data. Ordinarily, sampling consisted of high-frequency bursts at two hour intervals to capture surface waves, as well as more frequent measurements of tidal

currents and stage. At about 22:00 UT on 28 February 2010, sampling frequency was increased in anticipation of the arrival of the tsunami. An upward-looking acoustic Doppler current profiler (ADCP) collected current profiles averaged over 50 s from 3 m above the bed (mab) to the surface with 0.5 m vertical spacing, as well as water surface elevation, at 2-min intervals. A downward-looking Sontek pulse-coherent acoustic Doppler profiler (PCADP) collected near-bed current profiles and acoustic backscatter at 0.1 m vertical spacing from 0.08 to 0.55 mab at 1 Hz for 25 min out of every 30. A pressure sensor logged by the PCADP measured water surface elevation at the same frequency, resolving surface waves as well as the tsunami. A Sontek acoustic Doppler velocimeter (ADV) Hydra system measured velocity and pressure 0.16 mab at 4 Hz for 17 min every two hours, and for 120 s every 30 min.

[9] To characterize the tsunami fluctuations, tidal timescale variations were removed from the water surface elevations and velocities measured by the ADCP. Data from before the tsunami were interpolated to 2-min intervals, concatenated with the 2-min data during the tsunami, and filtered with a high-pass Butterworth filter (2 hr^{-1} pass band, 3 hr^{-1} stop band). Vertical velocities measured by the ADCP were not filtered, but were smoothed using a 3-point moving average.

[10] Data from pulse-coherent velocimeters must be corrected for ambiguity errors, which occur when velocities exceed the resolved range [*Lacy and Sherwood*, 2004]. To assist with this correction, the Sontek PCADP measures velocities (called resolution velocities) at a single point at relatively short range, where greater velocities can be resolved, before collecting each profile. For this data set we first corrected ambiguity errors in the resolution velocities, attributable to the high instantaneous speeds produced by the combination of surface waves and the tsunami. Then ambiguity errors in the current profiles were corrected as described in *Lacy and Sherwood* [2004]. To investigate currents and water surface elevation fluctuations associated with the tsunami, surface waves were removed from the PCADP data with a low-pass Butterworth filter (360 s^{-1} pass band, 240 s^{-1} stop band). Tidal variation in water surface elevation was removed by subtracting low-pass-filtered ADCP elevations.

[11] At times when a bottom boundary layer was visible in the data, friction velocity u_* associated with the tsunami was determined from the PCADP velocities based on the law of the wall. Logarithmic profiles were fit to 10-s averages of the low-pass-filtered north-south velocities in the three cells closest to the bed (centered 0.08–0.27 mab) using linear regression, and u_* and hydrodynamic roughness z_0 were determined by solving $v(z) = (u_*/\kappa)\log(z/z_0)$. To check whether a velocity profile from these three cells (the minimum number for regression) could reasonably be characterized as logarithmic, we applied two criteria: the coefficient of determination $R^2 > 0.985$, and 10^{-5} m $< z_0 < 10^{-2}$ m. u_* is only reported for profiles meeting these criteria.

[12] Suspended sediment concentrations were determined from the PCADP backscatter amplitude. Methods for calculating SSC from ADCP acoustic backscatter [*Wall et al.*, 2006] were adapted for the PCADP, an approach that has been validated by *Ha et al.* [2011] and *Yu et al.* [2011]. Measured SSC at one elevation is required for calibration. We used SSC calculated from ADV backscatter ($R^2 = 0.76$), which had in turn been calibrated to 10 days of SSC measurements by a laser in-situ scattering and transmissometry particle size analyzer (LISST) at the same elevation ($R^2 = 0.49$). Acoustic backscatter was not corrected for sediment attenuation α_s. For the median grain size in suspension of 100–150 μm (measured by the LISST), α_s is less than water attenuation for SSC less than 1 g/L [*Ha et al.*, 2011]. The error (an underestimate of SSC) introduced by neglect of α_s was estimated as less than 5% for these data.

[13] Surface wave statistics (significant wave height H_s, representative bottom orbital velocity u_{br}, wave period T, and wave direction) were calculated from the velocity and depth data from the PCADP bursts as well as the 17-min ADV bursts, following *Madsen* [1994]. Wave shear stress was estimated using a wave friction factor (f_w) approach [*Nielsen*, 1992]:

$$\tau_w = (1/2)\rho f_w u_{br}^2$$
$$f_w = \exp\left[5.213(k_b/A)^{0.194} - 5.977\right] \quad (1)$$

where A is the orbital amplitude and k_b is a roughness length scale. A k_b value of 0.72 cm was used, based on $k_b = 8\gamma^2/\lambda$ [*Nielsen*, 1992], and typical values of ripple wavelength λ and height γ observed at the site. Temporal variation in ripple roughness was not accounted for.

[14] We used singular-spectrum analysis (SSA) [*Vautard et al.*, 1992] to identify the primary frequencies of oscillation in water surface elevation and currents. SSA essentially applies principal components analysis to lagged segments of a single time series, by determining the eigenvectors of the covariance matrix of the lagged times series. The eigenvalue associated with each eigenvector (or component) corresponds to its proportion of the total variance. Periodic elements of the signal produce pairs of nearly equal eigenvalues and components. Frequencies of the pairs of reconstructed components were determined by counting zero-crossings. The amplitudes of the components can vary in time, making SSA well suited to the intermittent oscillations produced by tsunamis. The frequencies detected by SSA depend on the length of window that defines the matrix of lagged time series. We applied SSA in two steps. In the first step, the window was 200 min, to examine the low-frequency (tidal timescale) variation in the time series. The second or residual SSA used a window of 60 min, to identify frequencies in the range of the fundamental frequencies for Monterey Bay, i.e. 10–60 min periods [*Breaker et al.*, 2010].

3. Results

3.1. Overview

[15] The tsunami originating in Chile arrived in Monterey Bay at 20:36 on 27 February 2010 UT. At this time, tidal stage was falling. Surface-wave height and period increased between 12:00 on 27 February and 24:00 on 28 February. During the last four hours of 27 February significant wave height H_s was 1.3 m, representative bottom orbital velocity u_{br} was 0.4–0.5 m/s, representative wave period T_r was 10 s and wave direction was 185–190°.

[16] As tsunamis propagate from the source to far-field coastal regions, they are transformed first by dispersion,

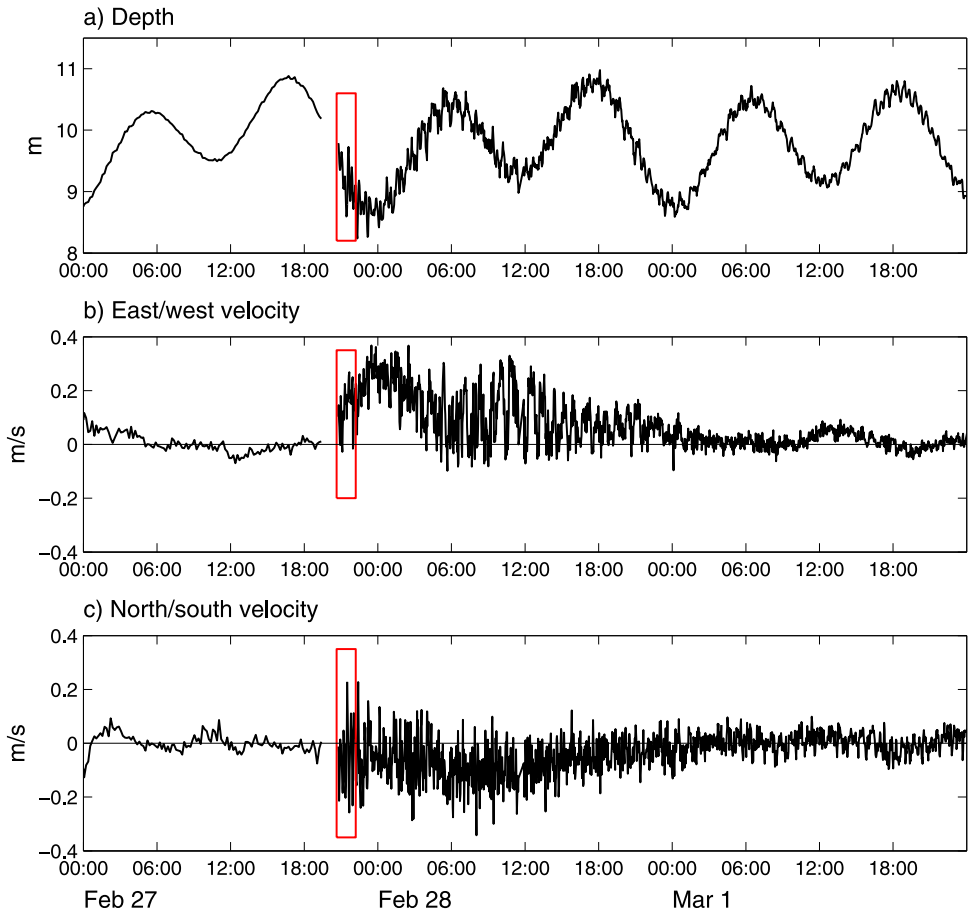

Figure 2. Time series of (a) water depth, (b) depth-averaged east-west velocity, and (c) depth-averaged north-south velocity, 27 February–1 March 2010, showing fluctuations created by the tsunami and subsequent seiching. Red boxes show the interval included in Figures 3 and 6.

refraction, and reflection, and then by local bathymetry [*Tang et al.*, 2008]. As a result, the first tsunami wave rarely has the greatest amplitude. In Monterey Bay, the effects of the Chile tsunami can be divided into two phases. The first phase (a couple of hours) was dominated by the incoming tsunami waves, with heights up to 1.1 m. The second phase constituted a local response to the perturbation of the tsunami, and consisted of trapped waves which persisted for several days, as well as enhanced tidal-timescale currents (Figure 2). This sequence of incident tsunami waves followed by resonant secondary undulations is typical in coastal bays [*Murty*, 1977], and seiching has been observed in Monterey Bay following previous large earthquakes [*Breaker et al.*, 2009]. Although fluctuations in water surface elevations, cross-shore velocities, and acceleration were greatest during the initial tsunami waves, the secondary response produced greater along-shore currents and total transport.

3.2. Characteristics of the Incident Tsunami Waves

[17] The first five oscillations in water surface elevation η produced by the tsunami had an average period T_t of 16 min. The fourth wave was the largest, with a local crest-to-trough height H_t of 1.12 m (0.56 m amplitude). Propagation speed C was approximately 9.4 m/s, estimated as $C = \sqrt{gh}$, where g is gravitational acceleration and h is water depth. Wavelength $\lambda_t = T_t\sqrt{gh}$ was 9 km; the approximately 800-m distance from the study site to shore was less than 0.1 λ_t. These results are specific to the depth of the study site, because the height, propagation speed, and maximum current speed of tsunami waves change rapidly with decreasing depth, as the tsunami approaches land.

[18] During the initial oscillations, the tsunami currents were directed north-south (cross shore). North-south velocity v was highly correlated with η during the first five oscillations, with a phase shift of approximately 90° (Figures 3a and 3b). High-pass-filtered v led η by 4 min in the ADCP data. In the PCADP data, low-pass-filtered v led η by an average of 262 s. Maximum depth-averaged v reached 0.36 m/s during the largest tsunami wave (Figure 3b). Depth-averaged smoothed vertical velocities w measured by the ADCP led η by 2–3 min, and had a maximum magnitude of 0.02 m/s (Figure 3d). There were no evident tsunami-related fluctuations in the near-bed w measured by the PCADP.

3.3. Variation of Tsunami Currents With Depth

[19] Profiles of v during the two largest oscillations (21:20–22:00) incorporating data from both the PCADP and the ADCP, are shown in Figure 4. At low speeds, and at times of rapid acceleration or deceleration, the velocities are quite constant with depth. During the periods of peak onshore or

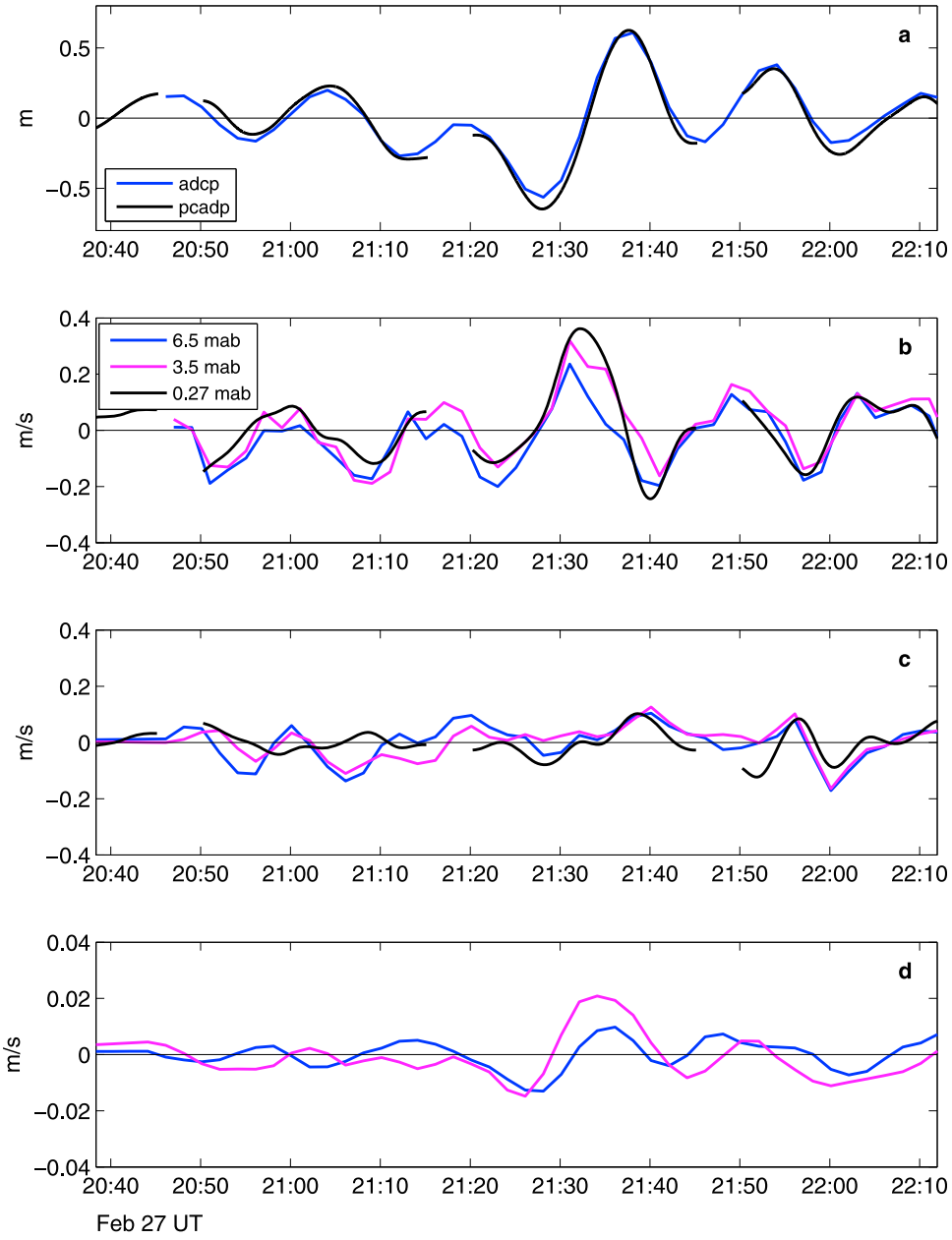

Figure 3. Time series of water surface elevation and currents during the tsunami, measured by the ADCP and PCADP: (a) water surface elevation η, tidal signal removed, (b) north-south velocities at 6.3, 3.5, and 0.27 mab, (c) east-west velocities at 6.3, 3.5, and 0.27 mab, and (d) vertical velocities at 6.3 and 3.5 mab, 3-point moving average.

offshore currents, strong shear developed in the bottom boundary layer and persisted during the deceleration of the wave (Figure 4b). In addition, during the strongest onshore currents, significant shear developed in the upper water column. At the peak of the onrush the maximum velocity was measured at the top of the PCADP profile (0.55 mab), and velocity was likely greater in between the elevation ranges of the PCADP and the ADCP. The cause of the shear in the upper water column is not known. Time-series plots of v at several elevations confirm that the velocities in the upper and mid water column track the near-bed velocities closely, except during the peak of the largest onrush (Figure 3b).

[20] Frictional damping can be seen at the bottom of the PCADP velocity profiles 2–3 min after the beginning of the largest onrush (Figures 5a and 5c). A logarithmic near-bed velocity profile, characteristic of steady flow over a rough bottom, developed and persisted for five min when the currents were strongest. Friction velocity u_* due to the tsunami was estimated for profiles with a logarithmic region at least 0.27 m thick (see Methods). Estimated u_* reached a maximum of 0.019 m/s, with a 90% confidence interval of 2.6×10^{-3} m/s (Figure 5b). At the time of maximum u_*, estimated z_0 was 2×10^{-4} m (90% CI $1.57–2.67 \times 10^{-4}$ m). This value of z_0 reflects the influence of surface waves as well as the

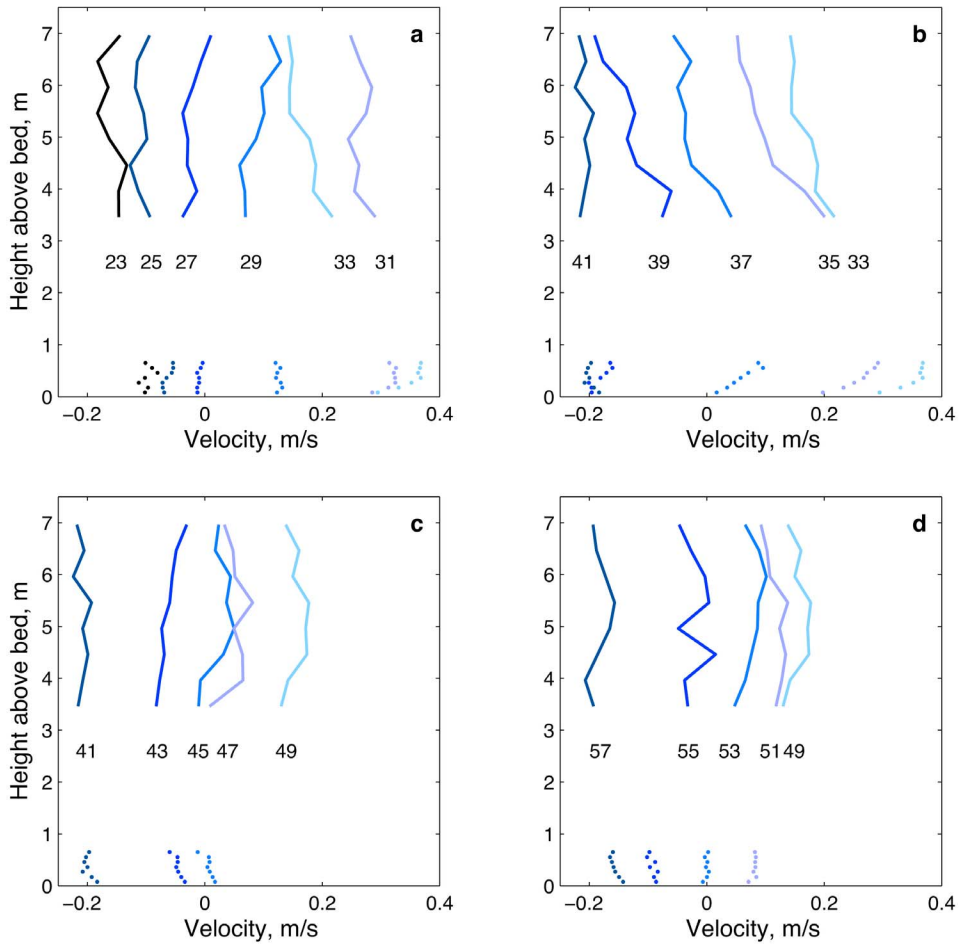

Figure 4. North-south velocity profiles (tides removed) at 2-min intervals during the two largest tsunami oscillations (21:20–22:00). Near-bed data from the PCADP (dots), upper water column from ADCP, with common color indicating synchronicity. Time of profiles shown in minutes after 21:00. Last profile in each of the first three subplots is repeated as first profile in the following subplot. No PCADP data were collected from 21:45 to 21:50.

physical roughness of the seafloor. The total shear between 0.55 and 0.08 mab, as well as the thickness of the sheared layer, continued to increase during the deceleration of the onrush (Figure 5d).

3.4. Near-Bed Momentum Balance

[21] The momentum equation in the direction of propagation of the tsunami wave can be written as

$$\frac{\partial v}{\partial t} = -v\frac{\partial v}{\partial y} - g\frac{\partial \eta}{\partial y} + \frac{1}{\rho_0}\frac{\partial \tau}{\partial z} \qquad (2)$$

where v is the velocity in the y direction (northward), ρ_0 is water density, and τ is total shear stress. On the right-hand side, the first term represents advection of momentum due to gradients of v in the y direction, the second represents the pressure gradient, and the third represents the influence of bottom friction. Equation (2) neglects lateral and vertical advection of momentum, which are typically at least an order of magnitude less than horizontal advection in regions of gradually varying bathymetry. Density gradients are also assumed to be negligible.

[22] Acceleration and the first two terms on the right-hand side of equation (2) were estimated for the north-south low-pass-filtered PCADP velocities (v) during 20:00–22:00 on 27 February. The spatial gradients for the pressure and advective terms were estimated as the quotient of the respective temporal gradients and the tsunami propagation speed C. Both the acceleration and the pressure-gradient terms have magnitudes on the order of 10^{-3} m/s^2 (Figure 6). The maximum value of the advective term was two orders of magnitude less ($<5 \times 10^{-5}$ m/s^2) (not shown), and thus can be neglected.

[23] The frictional term is difficult to estimate due to the unsteady nature of the flow. Bed shear stress due to the tsunami was determined as $\tau_t = \rho u_*^2$ for times when u_* could be estimated from the logarithmic bottom boundary layer (Figure 5b). However, since the height of the logarithmic layer varied with time and was not always known, the vertical gradient in τ could not be determined. In a fully developed steady flow, the friction term depends directly

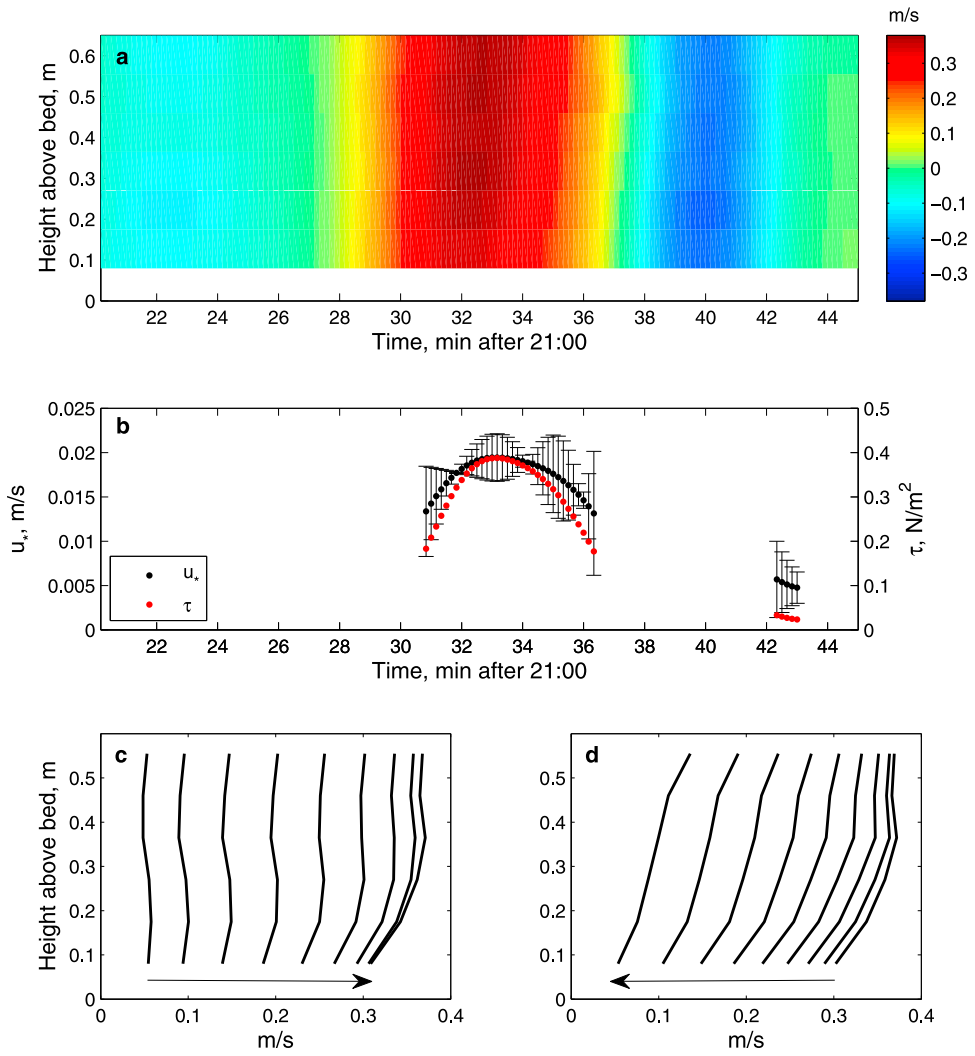

Figure 5. Bottom boundary layer currents during the largest tsunami wave. (a) Near-bed north-south low-pass velocity profiles from the 25-min PCADP burst starting at 21:20 on 27 February. (b) Friction velocity u_* and bed shear stress τ due to the tsunami currents, for times when the Figure 5a profiles were logarithmic. Error bars on u_* are 90% confidence intervals. (c) Profiles for 21:28–21:32 at 30-s intervals, illustrating development of logarithmic bottom boundary layer. (d) Profiles for 21:32.5–21:36.5 at 30-s intervals. Arrows indicate temporal progression.

on $v|v|$. In that case the pressure gradient is balanced by friction ($\partial v/\partial t = 0$), with the result that η lags v by 90°. In contrast, in an acceleration-pressure gradient balance that neglects friction (shallow water wave equation), η and v are in phase. Thus the 90° (on average) phase lag in these data confirms the significance of the friction term to the momentum balance. $v|v|$ is plotted in Figure 6d as an indicator of the frictional term in the momentum equation for quasi-steady flow.

[24] Peaks in $v|v|$ coincide with the peaks in the pressure gradient, and at these times acceleration is close to zero, indicating that the pressure gradient is balanced by drag (Figure 6). Peaks in the magnitude of $\partial v/\partial t$ occur both during the acceleration and deceleration phases. During acceleration, peaks in $\partial v/\partial t$ are opposite in sign to the pressure gradient and occur before the turbulent drag has developed enough to balance the pressure gradient. During deceleration, peaks in $\partial v/\partial t$ are the same sign as the pressure gradient and are produced by the lag in the decay of the turbulent drag relative to the decrease in the pressure gradient. This lag is characteristic of unsteady flow, and is not captured by $v|v|$ (Figure 6d).

[25] The lag between velocity and drag is illustrated by the relationship between friction velocity u_* and v (Figure 7). For a given v, the strength of turbulence as indicated by u_* is lower during acceleration than during deceleration. In steady, hydrodynamically rough flow the drag coefficient $C_d = u_*^2/V^2$ is constant for a given bed roughness, where V is the depth-averaged or reference velocity. In contrast, during the largest oscillation, C_d increased by almost an order of magnitude in 350 s, from 1.8×10^{-3} to 8.9×10^{-3} (using V at 0.55 mab). During the 40 s of peak velocity, C_d was fairly constant at $2.6 \pm 0.12 \times 10^{-3}$ (mean ± s.d.), a typical value for steady flow over sandy bottoms [*Sternberg*, 1968]. Closer to the bed the u_*/V ratio was greater and deceleration began sooner, reflecting the greater role of bed friction.

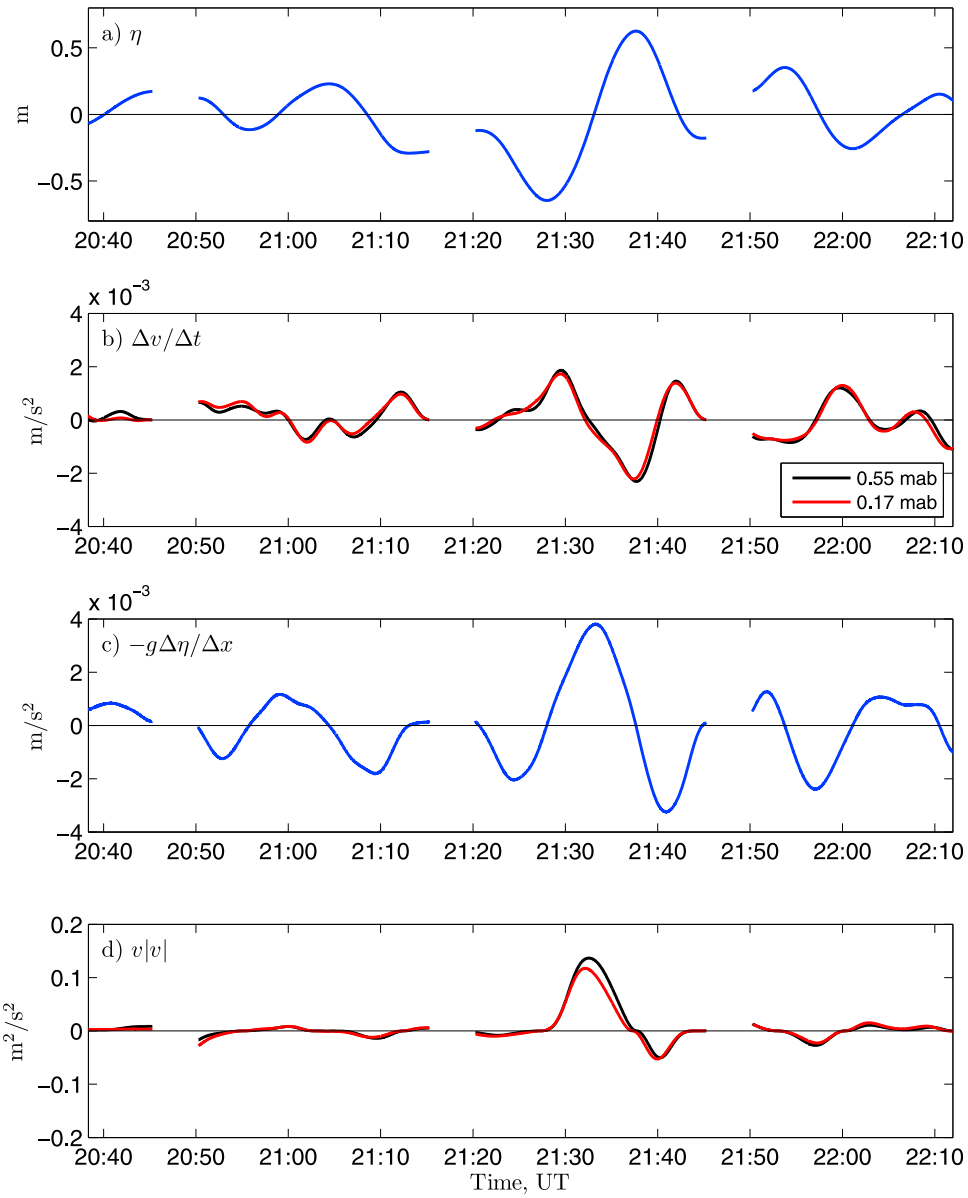

Figure 6. Time series of water surface elevation and estimates of several terms in the momentum equation for the near-bed north-south velocity, during the first two hours of the tsunami: (a) water surface elevation η (tides removed), (b) acceleration $\Delta v/\Delta t$, (c) pressure gradient $-g\Delta\eta/\Delta x$, and (d) $v|v|$, an indicator of friction for steady flow.

We observed similar hysteresis between velocity and friction velocity during a water surface oscillation following the 2009 Samoa tsunami (Figure 7b), although the maximum C_d was greater, perhaps due to the shorter period of the oscillation.

[26] The persistence of turbulent drag can produce a reversal of flow direction with depth at the end of the deceleration phase, because the drag force (directed opposite to the direction of flow) causes velocities close to the bed to change direction before $\partial\eta/\partial x$ changes sign. At the end of the strongest onrush, the velocity at the lowest point in the PCADP profiles reversed direction 30 s before the top of the PCADP profile and more than 60 s before the lowest point in the ADCP profile (Figure 8). An important consequence of this phenomenon is that during the interval of flow reversal, the direction of bed shear stress is opposite to that of the mean flow.

[27] The importance of accounting for friction in hydrodynamic modeling depends on the thickness of the bottom boundary layer. For a steady flow ($\partial v/\partial t = 0$), the thickness of a developing turbulent boundary layer can be estimated as

$$\delta = \sqrt{\nu_t t} \tag{3}$$

where ν_t is eddy viscosity and t is elapsed time [*Kundu*, 1990]. In a logarithmic boundary layer over a rough bottom, $\nu_t = \kappa u_* z$ near the bed, where z is height above the bed and $\kappa = 0.41$ is the von Kármán constant. Based on equation (3), the time required for the boundary layer to develop to a detectable

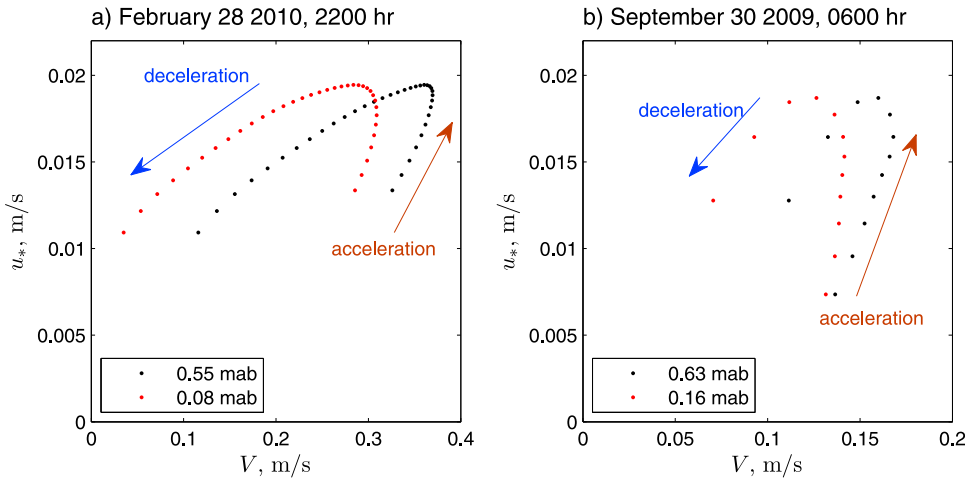

Figure 7. Friction velocity u_* vs. reference velocity V from two elevations above the bed at 10-s intervals. (a) Largest oscillation during Chile tsunami, with H = 1.1 m and T_t = 16 min. (b) Oscillation during Samoa tsunami with H = 0.2 m and T_t = 10 min.

thickness (δ = 0.27 m) is about 2 min, using z = 0.15 m and u_* = 0.01 m/s. During the largest oscillation, a logarithmic boundary layer with δ > 0.3 m was present for about 300 s. Based on the average u_* during this period of 0.017 m/s and ν_t at z = 0.3 m, the thickness of the logarithmic boundary layer predicted by equation (3) increases from 0.35 to 0.79 m between t = 1 min and t = 5 min. These calculations neglect the dependence of ν_t on δ, and thus overestimate δ at the beginning and underestimate it at the end. The observations of shear developing throughout the PCADP profiles during the strongest onrush are consistent with these estimates (Figure 5c). Although the maximum δ in this case is only about 10% of the water depth, this percentage increases as the tsunami approaches shore, and would be greater for large oscillations.

3.5. Bed Shear Stress and Sediment Transport

[28] Maximum bed shear stress produced by the tsunami currents τ_t was 0.4 N/m^2 (Figure 5b). During the largest oscillation the critical shear stress τ_c = 0.26 N/m^2 for the mean grain size at the site (315 μm) was exceeded for 4 min. The maximum bed shear stress exceeded τ_c = 0.36 N/m^2 for 435-μm particles (one standard deviation above the mean), indicating that the tsunami could mobilize essentially the entire distribution of grain sizes on the bed. However, at the time of the tsunami the surface waves were also quite energetic, and bed shear stress due to waves τ_w was approximately 2.5 N/m^2, almost five times greater than τ_t. Both the tsunami and the surface waves were directed to the north, and the maximum combined wave-tsunami bed shear stress was 2.9 N/m^2.

[29] Near-bed suspended sediment concentrations were relatively high during the tsunami (>1 g/L) (Figure 9b), but comparison with SSC late the previous day, when τ_w was similar (~2.5 N/m^2), indicates that the tsunami did not increase SSC in the meter above the seafloor over the level expected from wind-wave driven resuspension (Figures 9a, 9b and 10a). It did enhance cross-shore sediment transport, because of the strong tsunami-generated currents. Instantaneous cross-shore suspended sediment flux (SSF) (the product

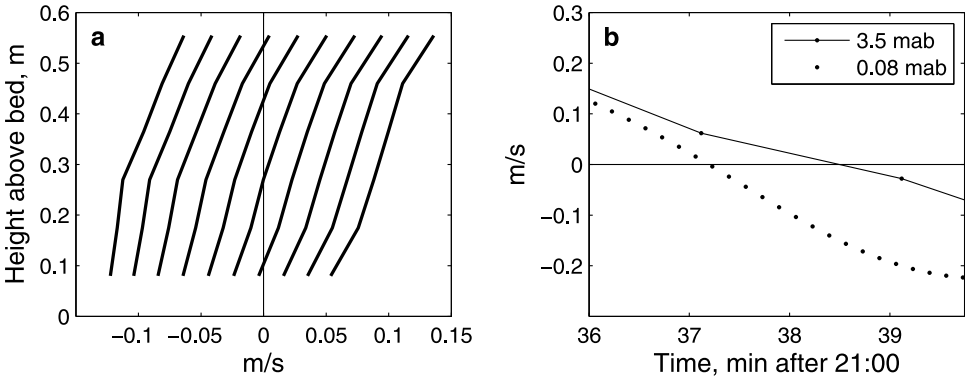

Figure 8. Flow reversal in the bottom boundary layer at the end of the onrush of the largest tsunami oscillation. (a) Profiles at 10-s intervals for 21:36.5–21:38 from PCADP burst in Figure 5a. Arrow indicates temporal progression. (b) Tsunami currents at 3.5 mab (ADCP) and 0.08 mab (PCADP) for 21:36–21:40.

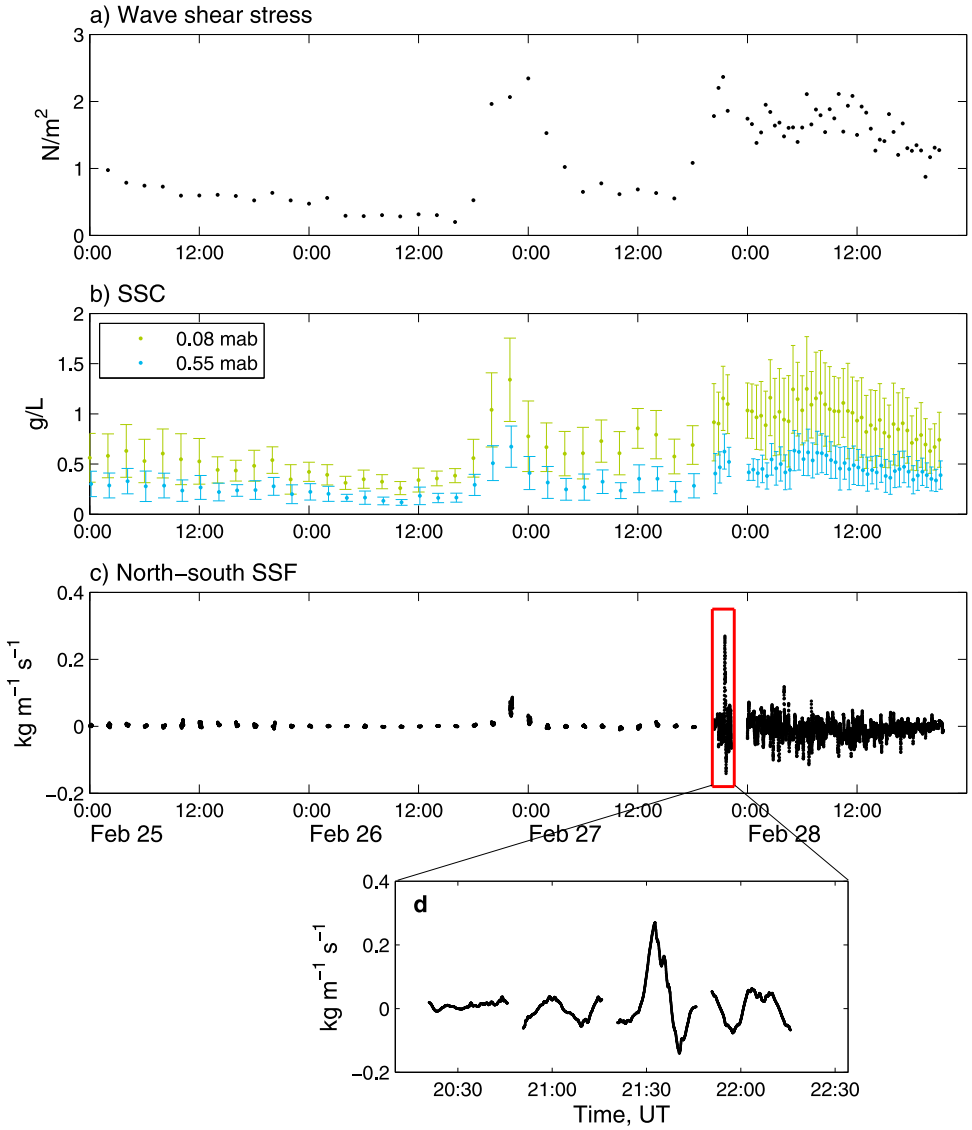

Figure 9. Time series of (a) wave shear stress, (b) suspended sediment concentration (SSC), and (c) north-south suspended sediment flux (SSF), 25–28 February 2010, and (d) detail of north-south SSF during initial tsunami oscillations.

of velocity and SSC) was more than three times greater at the peak of the strongest tsunami onrush than during the wave event on 26 February (Figures 9c and 9d). Onshore wave-driven currents at the time were less than 0.1 m/s, which is typical for wave events at this site. The magnitude of instantaneous SSF remained elevated during the days following the tsunami due to strong seiche currents.

3.6. Basin Response

[30] To better characterize the response to the tsunami over several days, we identified the primary frequencies of oscillation in η and depth-averaged east-west (u) and north-south (v) currents using singular-spectrum analysis. *Breaker et al.* [2011] used both SSA and ensemble empirical mode decomposition to identify the importance of fundamental frequencies in the oscillations produced by the Chile tsunami in data from the tide gauge in Moss Landing Harbor in central Monterey Bay. Our goals were to determine whether the frequencies identified by *Breaker et al.* [2011] also dominated η at our study site, and to determine the influence of the seiching on currents.

[31] The first step of the sequential SSA used a 200-min window. Variations at frequencies lower than 0.5 cycles/hr (Figure 11) were captured in the first two reconstructed components (RC). For η, RC1 and RC2 accounted for 97.2% of the total variance, and were clearly dominated by tidal fluctuations. This was not the case for u and v. Low-frequency u approached 0.3 m/s following the initial sequence of tsunami waves, much greater than the tidal currents at the site, which do not exceed ±0.05 m/s (Figure 11b), or wind-wave driven currents, which did not typically exceed 0.1 m/s during the 18 months of observations. The timing of the first peak in u suggests that it resulted from setup produced by the initial tsunami waves. The second peak in u coincides with a period of very large oscillations in u, apparently created by constructive interference of 51-min

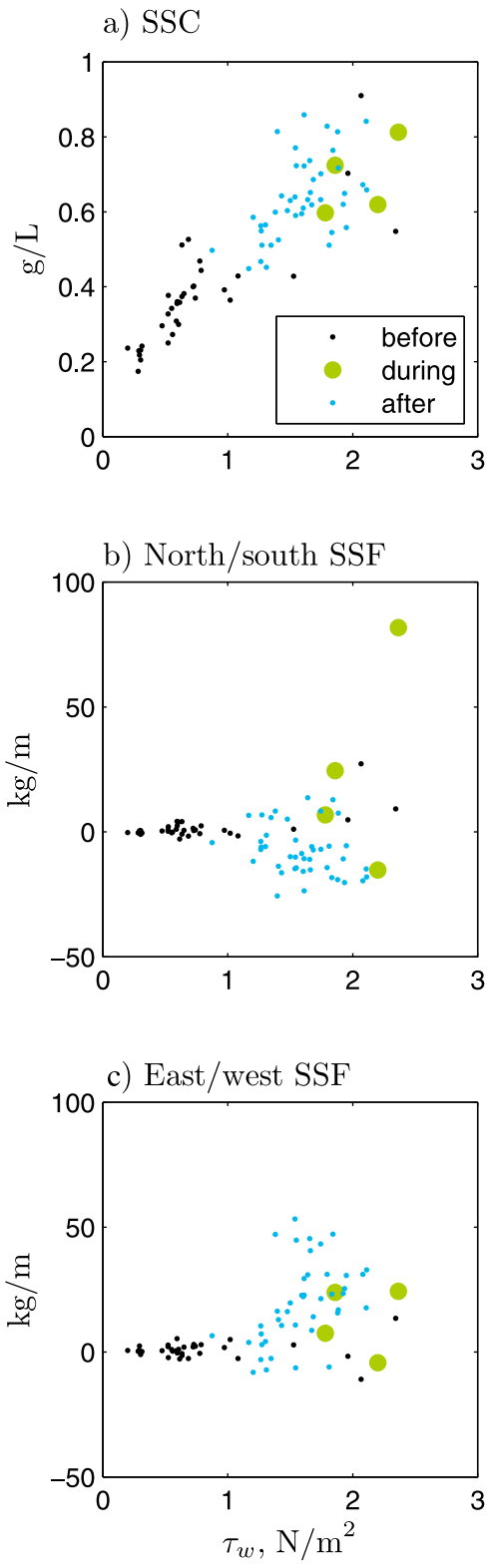

Figure 10. (a) Suspended sediment concentration (SSC) vs. shear stress due to surface waves τ_w. (b) 10-min cumulative north-south suspended sediment flux (SSF) between 0 and 60 cmab vs. τ_w. (c) 10-min cumulative east-west SSF between 0 and 60 cmab vs. τ_w.

and 27-min oscillations (Figures 12b and 12e; discussed below). RC1 and RC2 accounted for a much greater percentage of the total variance in η and u than in v (Table 1).

[32] RC1 and RC2 were subtracted from the u, v, and η data for 27 February–2 March, and a second SSA with a window of 60 min was applied to the residuals, to identify the importance of frequencies close to the fundamental modes of Monterey Bay. Results for the first eight components (ordered by decreasing percent variance) are summarized in Table 2. For η there were three pairs (indicating periodicity) of reconstructed components (referred to as RCr for the residual SSA). The frequency of the most energetic oscillations (RCr1 and RCr2) was 0.0195 min^{-1} (period 51.4 min). This likely represents a Bay-wide seiche along the north-south axis, as the fundamental longitudinal period of oscillation for Monterey Bay is 50–55 min [*Breaker et al.*, 2010] (Figure 12a). The amplitude of this mode approached 0.2 m for more than 12 hours following the tsunami. The frequency of the second pair (RCr3 and RCr4) was 0.037 min^{-1} (period 25–29 min). This is likely a harmonic of the fundamental longitudinal mode, and this frequency was also identified by *Breaker et al.* [2011] in the Moss Landing data. The 17.1-min period of the third pair (RCr5 and RCr6) is consistent with the period of the initial tsunami oscillations, and appears to be a natural period of oscillation of water level at the Santa Cruz wharf [*Breaker et al.*, 2010]. In sum, the first six RCrs, which account for 83.8% of the residual variance in η, are associated with resonant frequencies of Monterey Bay, confirming that the post-tsunami undulations are seiching rather than random fluctuations. The remaining RCrs each accounted for less than 4%.

[33] The seiching produced measurable currents. All three of the most energetic frequencies in η appear in the RCr's for u and v, although their relative importance varies. The most energetic pair of components of v (RCr1 and RCr2) had the frequency of the initial tsunami waves (Figure 12i). This mode constituted RCr7 and RCr8 of u (Figure 12h). The fundamental longitudinal mode appears as RCr1 and RCr2 of u, and RCr3 and RCr4 of v (Figures 12b and 12c). For this mode, the maximum oscillations in v, which are expected to dominate a longitudinal seiche at this site (see Monterey Bay inset in Figure 1), were ±0.05 m/s and occurred during the first 12 hours following the tsunami. The maximum oscillations in u were twice as great, and occurred just before 12:00 on 28 February, coinciding with the second peak in low frequency u (Figure 11b). The 25–29 min period component of η appears in u as RCr3 and RCr4 and in v as RCr5 and RCr6 (Figures 12e and 12f). As with the fundamental mode, the temporal variation of v follows that of η, whereas that of u does not. Moreover, the range of frequencies was slightly broader for u than for η or v (Table 2).

[34] In total, 62.5% of the residual variance in u and 49.1% of the residual variance in v was associated with the seiche frequencies identified in η. RCr5 and RCr6 of u did not exhibit the frequencies dominating η (Table 2). Although the seiche-induced variance was greater for u than v, the similarity to the temporal pattern in magnitude of oscillations of η was much greater for v than for u, suggesting that the north-south currents were a more direct response to seiche-related gradients in η. Current oscillations at seiche frequencies had greater amplitudes than local tidal currents for hours at a stretch, and the same order of amplitude as

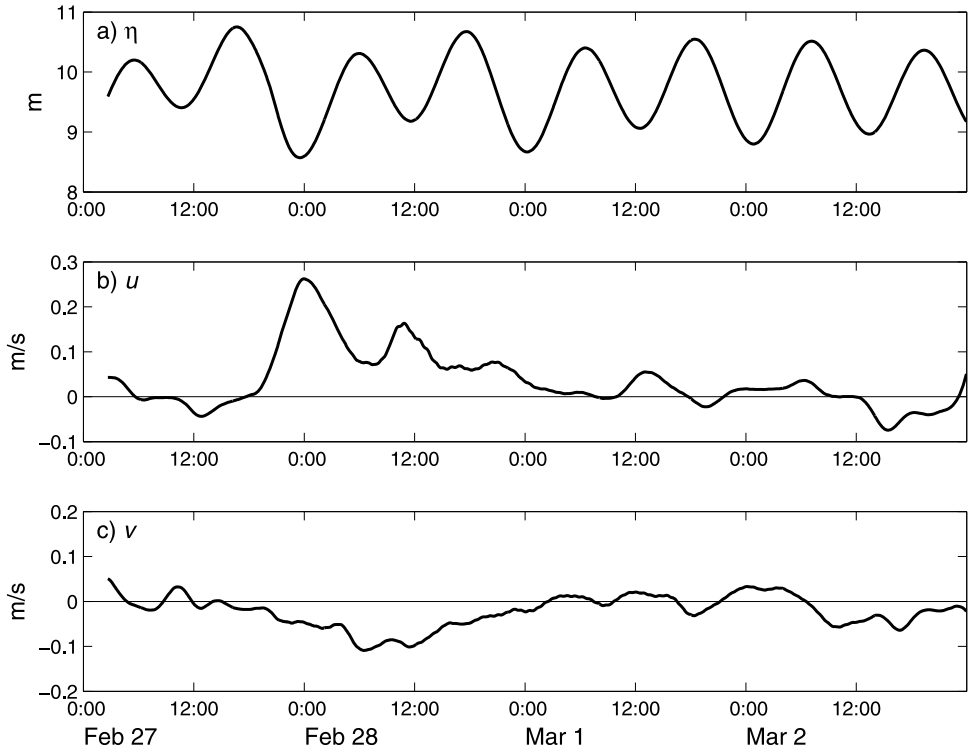

Figure 11. Sum of reconstructed components 1 and 2 for (a) η, (b) u, and (c) v from initial singular spectrum analysis (200-min window).

tidal currents for several days, indicating that the post-tsunami seiching constituted an important mixing and transport event.

4. Discussion

4.1. Quasi-steady and Unsteady Features

[35] Tsunami propagation across the deep ocean is typically modeled using the linear long-wave equation [*Murty*, 1977], in which both the advective and frictional terms of equation (2) are neglected:

$$\frac{\partial v}{\partial t} = -g\frac{\partial \eta}{\partial x} \tag{4}$$

This approximation requires that wavelength be much greater than water depth, which is the case for tsunamis even in the deep ocean. It also requires a ratio of wave height to water depth $H/h \ll 1$. Under these conditions frequency dispersion is minimal. Modeling of tsunamis as they approach shore, and H/h increases, requires more sophisticated models [*Lynett*, 2009]. A nonlinear form of the long-wave equation is used to account for advection and variation in wave celerity across the tsunami oscillation, which results in wave steepening. The inclusion of friction requires additional modifications. Depth-averaged models incorporate the effect of friction based on a drag law [*Liu et al.*, 1995; *Fujima et al.*, 2002; *Lynett*, 2009], assuming that the tsunami behaves as a steady or quasi-steady flow. Our data provide an opportunity to test this assumption.

[36] In a quasi-steady flow ($\partial v/\partial t$ negligible) the bottom boundary layer is logarithmic, and its height scales with depth-averaged speed, which results in a constant drag coefficient. When the observed tsunami currents and drag were strongest, the bottom boundary layer was logarithmic, although with time-varying thickness. The hysteresis between V and u_* (Figure 7) demonstrates that the drag coefficient was not constant. Use of an average drag coefficient for the period of maximum currents would produce reasonable values for maximum speed and total mixing, but would not accurately identify the timing of the maximum current or drag, or predict the greater turbulence and shear during deceleration than acceleration of the tsunami wave.

[37] At times of maximum acceleration and deceleration, the frictionally influenced boundary layer was very thin, and the flow cannot be characterized as steady. The flow reversal near the bed observed during deceleration is a feature of the unsteady nature of the flow. Treating the tsunami currents as quasi-steady during the deceleration of the largest observed oscillation would produce inaccurate estimates of the direction of stress on the bed, the torque exerted on objects resting on the bed, vertical variation in horizontal dispersion, and vertical mixing. The consequences of the assumptions of steady flow and a constant drag coefficient are relevant to modeling for the purpose of reconstructing current speed from paleo-tsunami deposits as well as for predicting tsunami impacts.

[38] The relative importance of the unsteady aspects of a tsunami wave depends on the tsunami period as well as its amplitude. Tsunamis exhibit a wide range of periods in coastal waters, ranging from 5 to 90 min [*Murty*, 1977]. Shorter periods allow less time for the bottom boundary layer to develop, while longer periods extend the interval of relatively steady flow. With greater amplitude, u_* and thus ν_t

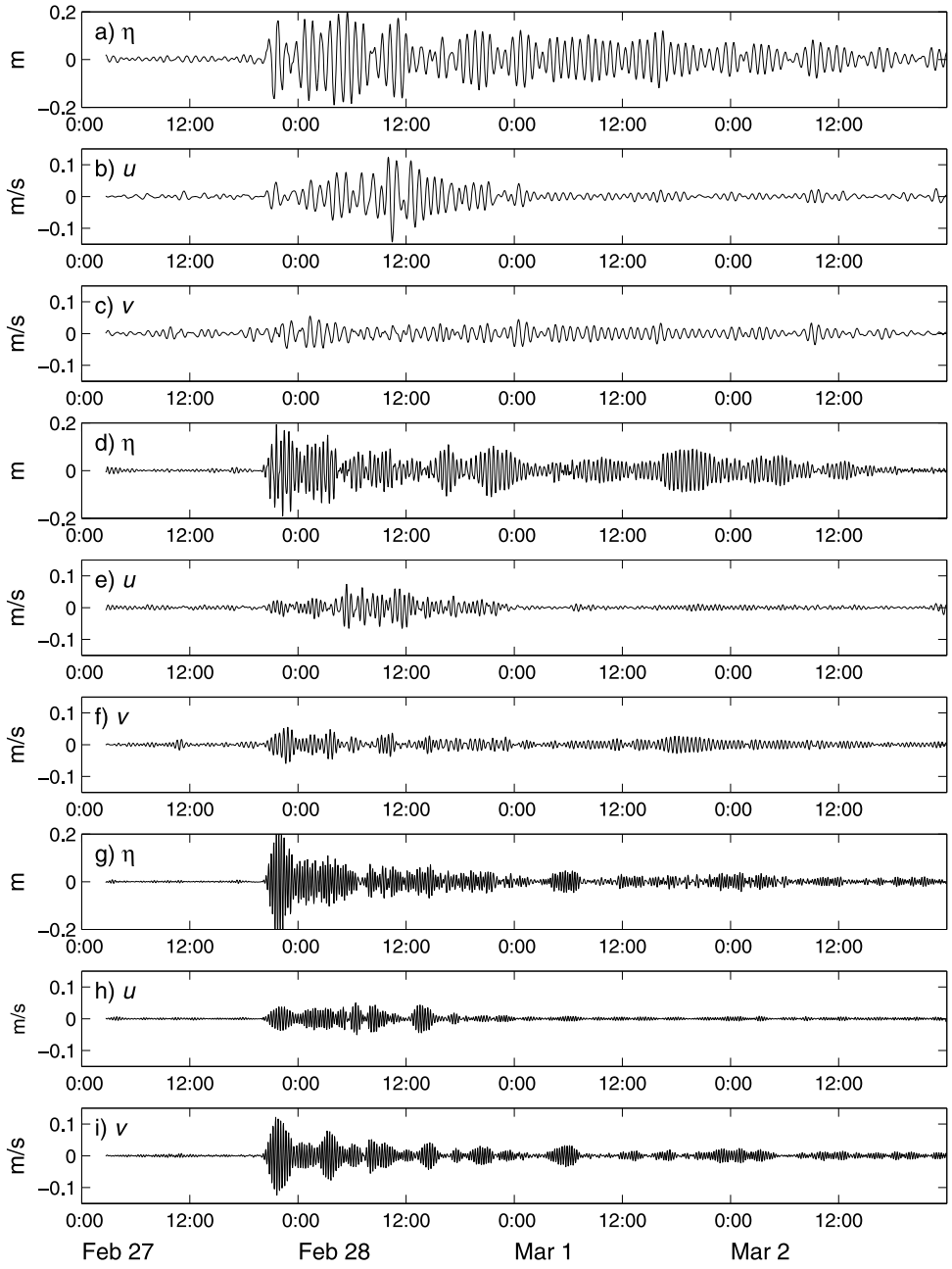

Figure 12. Reconstructed components (*RCr*) from the residual singular spectrum analysis (60-min window), grouped by frequency. $f = 3.243 \times 10^{-4}$ s^{-1} (51.4-min period): (a) η, *RCr*1 + *RCr*2, (b) *u*, *RCr*1 + *RCr*2, and (c) *v*, *RCr*3 + *RCr*4. $f = 6.173 \times 10^{-4}$ s^{-1} (27-min period): (d) η, *RCr*3 + *RCr*4, (e) *u*, *RCr*3 + *RCr*4, and (f) *v*, *RCr*5 + *RCr*6. $f = 9.747 \times 10^{-4}$ s^{-1} (17-min period): (g) η, *RCr*5 + *RCr*6, (h) *u*, *RCr*5 + *RCr*6, and (i) *v*, *RCr*1 + *RCr*2.

are greater, resulting in more rapid growth of the bottom boundary layer (equation (3)).

4.2. Tsunami-Induced Sediment Transport

[39] The combination of the tsunami currents with the elevated SSC produced a strong pulse of onshore SSF (Figures 9c and 9d). To estimate the maximum gross transport caused by the tsunami, we calculated cumulative SSF for the 10-min duration of the strongest onrush. Cumulative onshore SSF in the 60 cm above the seafloor was 82 kg/m, approximately four times greater than during any other 10-min interval of 26 February–1 March (Figure 10b). The maximum northward water displacement ($\sum v\Delta t$) during this oscillation was 120 m, so 82 kg/m constitutes transport of 0.7 kg of sediment 120 m towards shore in the 60 cm above

Table 1. Percent Variance for First Two Reconstructed Components (RC) of the Initial SSA (200-min Window) for η, *u*, and *v*

RC	η	*u*	*v*
1	79.7	65.7	37.8
2	17.9	7.0	4.4

Table 2. Summary of Results From the Residual SSA (60-min Window) for η, u, and v[a]

	η		u		v	
RCr	f	σ^2	f	σ^2	f	σ^2
1	0.0195	21.8	0.0195	19.3	0.0585	11.4
2	0.0195	18.2	0.0195	19.1	0.0585	11.2
3	0.0375	13.2	0.0319	8.4	0.0195	8.1
4	0.0375	12.4	0.0361	7.2	0.0195	7.7
5	0.0571	9.4	–	5.1	0.0389	5.4
6	0.0571	8.9	0.0455	4.8	0.0361	5.3
7	–	3.6	0.0585	4.4	0.10	4.5
8	–	2.5	0.0585	4.1	0.10	4.2

[a]Frequency f in min^{-1} and percent variance σ^2 for the first 8 reconstructed components (RCr). Dash indicates nonperiodic component.

the seafloor, for every square meter of seafloor. Easterly SSF continued to increase in the aftermath of the tsunami, due to the easterly currents produced by the seiche. Although the rate of transport was greatest during the initial tsunami oscillations, the seiching produced greater cumulative SSF (Figure 10c).

[40] The estimates of sediment flux may underestimate the effect of the tsunami because they are limited to the near-bed region. Both the periods of strongest currents during the initial oscillations and elevated currents during the following days have the potential to mix suspended sediment higher up into the water column than during wave events with weak currents. Although not captured in our measurements, it is possible that increased vertical mixing increased the total mass of sediment in the water column and the total flux, depending on the grain size (settling speed) of the suspended particles.

[41] In assessing the mobilization of sediment by tsunamis it is important to consider local wave conditions. When the 2010 Chile tsunami arrived in Monterey Bay, the bed was already mobilized by surface waves. In contrast, the 2009 Samoa tsunami produced subcritical bed shear stress at the study site, and at that time wind-wave shear stress was also subcritical. However, the combination of the tsunami and the local waves exceeded the threshold for mobilization of the bed sediments. The presence of wind-waves also likely influence bed shear stress produced by tsunamis in the same way that they interact with other currents, by increasing apparent roughness [*Grant and Madsen*, 1979].

5. Conclusions

[42] These are the first reported field observations of tsunami-generated currents that include the near-bed region. In Monterey Bay, the 2010 Chile tsunami produced a series of cross-shore directed oscillations with period of approximately 16 min for the first couple of hours, followed by seiching with a range of frequencies and variable direction that lasted several days. The crest-to-trough height of the largest tsunami wave was 1.1 m and the maximum depth-averaged cross-shore current speed was 0.36 m/s at the 10-m deep study site. During the initial tsunami waves, velocities led water surface elevation (η) by 90°, and at times of maximum current speed a logarithmic bottom boundary layer developed with thickness greater than 0.3 m. During the strongest currents the average drag coefficient C_d was 2.6×10^{-3}, a typical value for a sandy seafloor. However, C_d varied by an order of magnitude within 5 min, because turbulence intensity (u_*) lagged current speed. Turbulent diffusion of momentum and boundary layer thickness continued to increase into the deceleration phase of the wave. At the end of the strongest onrush flow reversal occurred near the bed. Near-bed velocity and bed shear stress were directed opposite to the depth-averaged velocity for 60 s. During the maximum onrush and offrush, the currents generated by the tsunami can be characterized as quasi-steady, but at other phases acceleration is significant to the near-bed momentum, and bed drag is not in phase with the mean flow. This unsteady behavior cannot be simulated by tsunami models that rely on a quadratic drag law.

[43] The largest tsunami wave produced sufficient bed shear stress to mobilize the medium-grained sand bed of the study site. The tsunami did not enhance near-bed suspended sediment concentrations because at the time it arrived, wind waves with 1.3 m significant height exerted a much greater shear stress on the bed. Nonetheless, cross-shore suspended sediment flux was enhanced, because of the strength and duration of the tsunami currents.

[44] Seiching occurred in Monterey Bay for several days following the arrival of the tsunami. The most energetic seiche frequency was 0.0195 min^{-1} (51.4 min period), the fundamental longitudinal frequency of Monterey Bay. Oscillations at three natural frequencies accounted for 84% of the variance in supertidal (tides removed) η, 63% of the variance in supertidal u, and 49% of the variance in supertidal v during 27 February–2 March. The greatest current oscillations (0.18 m/s amplitude) were in the alongshore (east-west) direction, and were produced by constructive interference of modes with 51.4 min and 27 min periods. Easterly hourly-timescale currents approached 0.3 m/s within hours of the tsunami arrival, the strongest at this site in 18 months of observations. Maximum hourly-timescale sediment flux also occurred at this time, although instantaneous flux was greater during the initial tsunami waves.

[45] **Acknowledgments.** Gerry Hatcher, Rob Wyland, Pete DalFerro, Jamie Grover, Curt Storlazzi, Josh Logan, George Tate, Tim Elfers, and Kevin O'Toole assisted with development, installation, and maintenance of the Santa Cruz seafloor observatory, where the data were collected. Special thanks to Gerry Hatcher for adjusting the sampling frequencies on short notice to capture the tsunami. Shandy Buckley assisted with data processing, and Theresa Fregosa made Figure 1. Thanks to Eric Geist for helpful discussions and advice on the state of tsunami modeling. Eric Geist, Robert Weiss, and an anonymous reviewer provided helpful comments on the manuscript. Any use of trade, product, or firm names in this paper is for descriptive purposes only and does not imply endorsement by the U.S. Government.

References

Allan, J. C., P. D. Komar, P. Ruggiero, and R. Witter (2012), The March 2011 Tohoku tsunami and its impacts along the U.S. West Coast, *J. Coastal Res.*, doi:10.2112/JCOASTRES-D-11-00115.1, in press.

Breaker, L. C., T. S. Murty, J. G. Norton, and D. Carroll (2009), Comparing sea level response at Monterey, California from the 1989 Loma Prieta earthquake and the 1964 great Alaskan earthquake, *Sci. Tsunami Hazards*, *28*(5), 255–271.

Breaker, L. C., Y. Tseng, and X. Wang (2010), On the natural oscillations of Monterey Bay: Observations, modeling, and origins, *Prog. Oceanogr.*, *86*, 380–395, doi:10.1016/j.pocean.2010.06.001.

Breaker, L. C., T. S. Murty, S. J. Flora, and C. N. Hunter (2011), The response of Monterey Bay to the 2010 Chilean earthquake, *Sci. Tsunami Hazards*, *30*(1), 1–23.

Bricker, J. D., S. Munger, C. Pequignet, J. R. Wells, G. Pawlak, and K. F. Cheung (2007), ADCP observations of edge waves off Oahu in the wake of the November 2006 Kuril Islands tsunami, *Geophys. Res. Lett.*, *34*, L23617, doi:10.1029/2007GL032015.

Dengler, L., B. Uslu, A. Barberopoulou, S. C. Yim, and A. Kelly (2009), The November 15, 2006 Kuril Islands–generated tsunami in Crescent City, California, *Pure Appl. Geophys.*, *166*, 37–53, doi:10.1007/s00024-008-0429-2.

Fritz, H. M., J. C. Borrero, C. E. Synolakis, and J. Yoo (2006), 2004 Indian Ocean tsunami flow velocity measurements from survivor videos, *Geophys. Res. Lett.*, *33*, L24605, doi:10.1029/2006GL026784.

Fritz, H. M., D. A. Phillips, A. Okayasu, T. Shimozono, H. Liu, F. Mohammed, V. Skanavis, C. E. Synolakis, and T. Takahashi (2012), The 2011 Japan tsunami current velocity measurements from survivor videos at Kesennuma Bay using LiDAR, *Geophys. Res. Lett.*, *39*, L00G23, doi:10.1029/2011GL050686.

Fujima, K., K. Masamura, and C. Goto (2002), Development of the 2D/3D hybrid model for tsunami numerical simulation, *Coastal Eng. J.*, *44*(4), 373–397.

Grant, W. D., and O. S. Madsen (1979), Combined wave and current interaction with a rough bottom, *J. Geophys. Res.*, *84*(C4), 1797–1808.

Ha, H., J.-Y. Maa, K. Park, and Y. Kim (2011), Estimation of high-resolution sediment concentration profiles in bottom boundary layer using pulse-coherent acoustic Doppler profilers, *Mar. Geol.*, *279*, 199–209, doi:10.1016/j.margeo.2010.11.002.

Huntington, K., J. Bourgeois, G. Gelfenbaum, P. Lynett, B. Jaffe, H. Yeh, and R. Weiss (2007), Sandy signs of a tsunami's onshore depth and speed, *Eos Trans. AGU*, *88*(52), 577.

Kundu, P. K. (1990), *Fluid Mechanics*, Academic, San Diego, Calif.

Lacy, J., and C. Sherwood (2004), Accuracy of a pulse-coherent acoustic doppler profiler in a wave dominated environment, *J. Atmos. Oceanic Technol.*, *21*(9), 1448–1461.

Liu, P. L.-F., Y.-S. Cho, M. J. Briggs, U. Kanoglu, and C. E. Synolakis (1995), Runup of solitary waves on a circular island, *J. Fluid Mech.*, *302*, 259–285.

Lynett, P. J. (2009), Modeling of tsunami inundation, in *Encyclopedia of Complexity and Systems Science*, edited by R. A. Meyers, pp. 9618–9631, Springer, New York, doi:10.1007/978-0-387-30440-3_569.

Lynett, P. J., J. C. Borrero, R. Weiss, S. Son, D. Greer, and W. Renteria (2012), Observations and modeling of tsunami-induced currents in ports and harbors, *Earth Planet. Scie. Lett.*, *327–328*, 68–74, doi:10.1016/j.epsi.2012.02.002.

Madsen, O. S. (1994), Spectral wave-current bottom boundary layer flows, in *Proceedings of the 24th International Conference on Coastal Engineering*, pp. 384–398, Am. Soc. of Civ. Eng., New York.

Miles, J. W. (1974), Harbor seiching, *Annu. Rev. Fluid Mech.*, *6*, 17–33.

Munger, S., and K. F. Cheung (2008), Resonance in Hawaii waters from the 2006 Kuril Islands tsunami, *Geophys. Res. Lett.*, *35*, L07605, doi:10.1029/2007GL032843.

Murty, T. S. (1977), *Seismic Sea Waves: Tsunamis*, *Bull. Fish. Res. Board Can.*, *198*, 337 pp.

Nielsen, P. (1992), *Coastal Bottom Boundary Layers and Sediment Transport*, World Sci., Singapore.

Sternberg, R. W. (1968), Friction factors in tidal channels with varying bed roughness, *Mar. Geol.*, *6*(3), 243–260.

Tang, L., et al. (2008), Tsunami forecast analysis for the May 2006 Tonga tsunami, *J. Geophys. Res.*, *113*, C12015, doi:10.1029/2008JC004922.

Vautard, R., P. Yiou, and M. Ghil (1992), Singular-spectrum analysis: A toolkit for short, noisy, chaotic signals, *Physica D*, *58*, 95–126.

Wall, G., E. Nystrom, and S. Litten (2006), Use of an ADCP to compute suspended-sediment discharge in the tidal Hudson River, New York, *U.S. Geol. Surv. Sci. Invest. Rep.*, *2006-5055*.

Yeh, H. (2006), Maximum fluid forces in the tsunami runup zone, *J. Waterw. Port Coastal Ocean Eng.*, *132*(6), 496–500.

Yu, J., J. Jiang, D. Gong, S. Li, and Y. Xu (2011), Determining suspended sediment concentration and settling velocity from PC-ADP measurements in the Beibu Gulf, China, *Chin. J. Oceanol. Limnol.*, *29*(3), 691–701, doi:10.1007/s00343-011-0164-x.